Supporting Information

Enhanced ORR Activity of Carbon Defects via Substituent-modulated Electronic Perturbation.

Yun Han [1,2], Xin Mao [3], Xuecheng Yan [1], Qilong Wu [4], Qingchao Fang [3], Hanqing Yin [3], Yi Jia [5], Qin Li [1,2*], Xiangdong Yao [6*], Aijun Du [3*]*

Affiliations

[1] Queensland Micro- and Nanotechnology Centre, Griffith University, Nathan Campus, QLD 4111, Australia.

[2] School of Engineering and Built Environment, Nathan Campus, Queensland, 4111, Australia.

[3] School of Chemistry and Physics and Centre for Materials Science, Queensland University of Technology, Gardens Point Campus, Brisbane 4001, Australia.

[4] Intelligent Polymer Research Institute and ARC Centre of Excellence for Electromaterials Science, Australian Institute for Innovative Materials, University of Wollongong, Wollongong, NSW 2500, Australia.

[5] College of Chemical Engineering and Zhejiang Carbon Neutral Innovation Institute, Zhejiang University of Technology, Hangzhou 310032, P. R. China.

[6] School of Advanced Energy and IGCME, Sun Yat-Sen University (Shenzhen), Shenzhen, Guangdong 518107, P. R. China.

Computational Details:

Spin-polarized density functional theory (DFT) calculations in this work were mainly conducted by the Vienna Ab initio Simulation Package (VASP).[1, 2] The projector augmented wave (PAW) method was adopted to describe the core electron with a cut-off energy of 400 eV.[3] The exchange-correlation interactions were represented by Perdew-Burke-Ernzerhof (PBE) functional based generalized gradient approximation (GGA).[4, 5] Gaussian smearing of electronic occupations with a width of 0.1 eV and a gamma type (1, 1, 1) K-point mesh were used for Brillouin zone sampling. During all the optimization, the convergence thresholds were 10^{-5} eV and 10^{-2} eV/Å for energy and force, respectively. The Van der Waals interaction was described by the DFT+D3 method using empirical correction in Grimme's scheme.[6, 7] A series of graphene-based cluster type models were built to test the ORR activity, and vacuum space on each direction were set to be larger than 15 Å, avoiding interaction between periodical images. The Gaussian (G16) program was used to calculate the electronic structure of the models at B3LYP/6-31G* level.[8] Furthermore, VASPkit, Bader, and Multiwfn packages were used to assist the analysis of electronic structures,[9-11] VESTA and Atomic Simulation Environment (ASE) were adopted to build the models.[12, 13]

To assess the catalytic activity for oxygen reduction reaction (ORR), we considered the four-electron pathway, which is as follows:[14]

$$* + O_2 + H^+ + e^- \rightarrow *OOH \tag{S1}$$

$$*OOH + H^+ + e^- \rightarrow *O + H_2O \tag{S2}$$

$$*O + H^+ + e^- \rightarrow *OH \tag{S3}$$

$$*OH + H^+ + e^- \rightarrow * + H_2O \tag{S4}$$

The Gibbs free energy of O_2 is derived from $H_2O \rightarrow 1/2\,O_2 + H_2$ using the experimental reaction energy of 2.46 eV to avoid the limitations of DFT calculation in describing the high-spin ground state of O_2 molecule.[15] The Gibbs free energy of formation for the i_{th} ($i = 1, 2, 3,$ and 4) step was calculated using the following formula:

$$\Delta G_i = \Delta E_{DFT} + \Delta ZPE - T\Delta S - eU \qquad (S5)$$

where ΔE_{DFT}, represents the change in DFT total energy, while ΔZPE and $T\Delta S$ signify the variations in zero-point energy and entropy, respectively, during the reactions. T is temperature, U is the electrode potential, e is the electron charge transfer. In this work, the values of ($\Delta ZPE - T\Delta S$) for Eq. S1-S4 were adopted from previous works as they are not sensitive to the type of catalyst, and the specific values are listed in Table S11.[16]

The ORR overpotential is then given by:

$$\eta_{ORR} = \Delta G_{ORR}/e + U_0 \qquad (S6)$$

where $\Delta G_{ORR} = \max [\Delta G_1, \Delta G_2, \Delta G_3,$ and $\Delta G_4]$, and $U_0 = 1.23$ V is the equilibrium potential for pH = 0 and temperature $T = 298$ K.

Based on Eq. S1-S6, η_{ORR} can be obtained by computing the binding energies of relevant reaction intermediates on various sites of the catalyst surface. Here we refer the binding energies of all the reaction intermediates to those of H_2 and H_2O molecules as follow:

$$\Delta E_{ads}(*OOH) = E(*OOH) - E(*) - [2E(H_2O) - 3/2 E(H_2)] \qquad (S7)$$

$$\Delta E_{ads}(*O) = E(*O) - E(*) - [E(H_2O) - E(H_2)] \qquad (S8)$$

$$\Delta E_{ads}(*OH) = E(*OH) - E(*) - [E(H_2O) - 1/2 E(H_2)] \qquad (S9)$$

where $E(*)$, $E(*OOH)$, $E(*O)$, and $E(*OH)$ are the DFT total energies of a clean catalyst surface, and that adsorbed by a *OOH, *O, and *OH species, respectively. The binding energies of reaction intermediates on the FDCs models are provided in Table S2-S10.

The formation energies of FDCs are calculated through the following equation:

$$\Delta E_{FDCs} = E(FDCs) + 0.5*E(H_2) - E(DCs) - E(F) \qquad (S11)$$

in which, $E(FDCs)$, $E(DCs)$, and $E(F)$ are the DFT total energies of FDCs, defective carbons (DCs), and functional groups, respectively. Additionally, implicit water layers provided by VASPsol package were adopted during the DFT energies of functional groups.[17, 18]

When calculating the charge transfer volume (CT) and the HOMO distribution, the carbon atom adsorbed by the functional group is considered an integral component of the substituent. Consequently, the CT value is derived from the cumulative charge changes within the functional group and its associated carbon atoms. Similarly, the HOMO distribution value results from the summation of the HOMO contribution ratios pertaining to seven selected carbon active centers, excluding the one that adsorbs the functional group.

Unlike the open shell d bands of transition metals, there is a scarcity of available C p states in the conduction bands, and the antibonding states formed by C p orbitals are almost completely occupied.[19, 20] Therefore, the linear relationship between the binding strength and the $\mathcal{E}_p$ can be interpreted using the extended Hückel method developed by Roald Hoffmann[21]:

$$H_{ij} = 0.5KS_{ij}(H_{ii} + H_{jj}) \tag{S12}$$

Here, K represents the Wolfsberg-Helmholtz constant, typically assigned a value of 1.75. The orbital overlap matrix element, S_{ij}, depends on the distance between elements i and j. H_{ii} and H_{jj} correspond to the diagonal elements. In this case, S_{ij} can be considered as a constant since the C-O bond length remains nearly unchanged across different defective carbon models (within the range of 0.1 Å), H_{ii} and H_{jj} represent the absolute energy levels of the valence states of the carbon atoms acting as active sites and the adjacent oxygen atoms in the reaction intermediates, respectively. Thus, H_{ij} is mainly determined by the valence orbital levels of the carbon atoms. Deeper localization of the C p centers leads to lower H_{ij}, eventually resulting in stronger binding strength with the reaction intermediates.
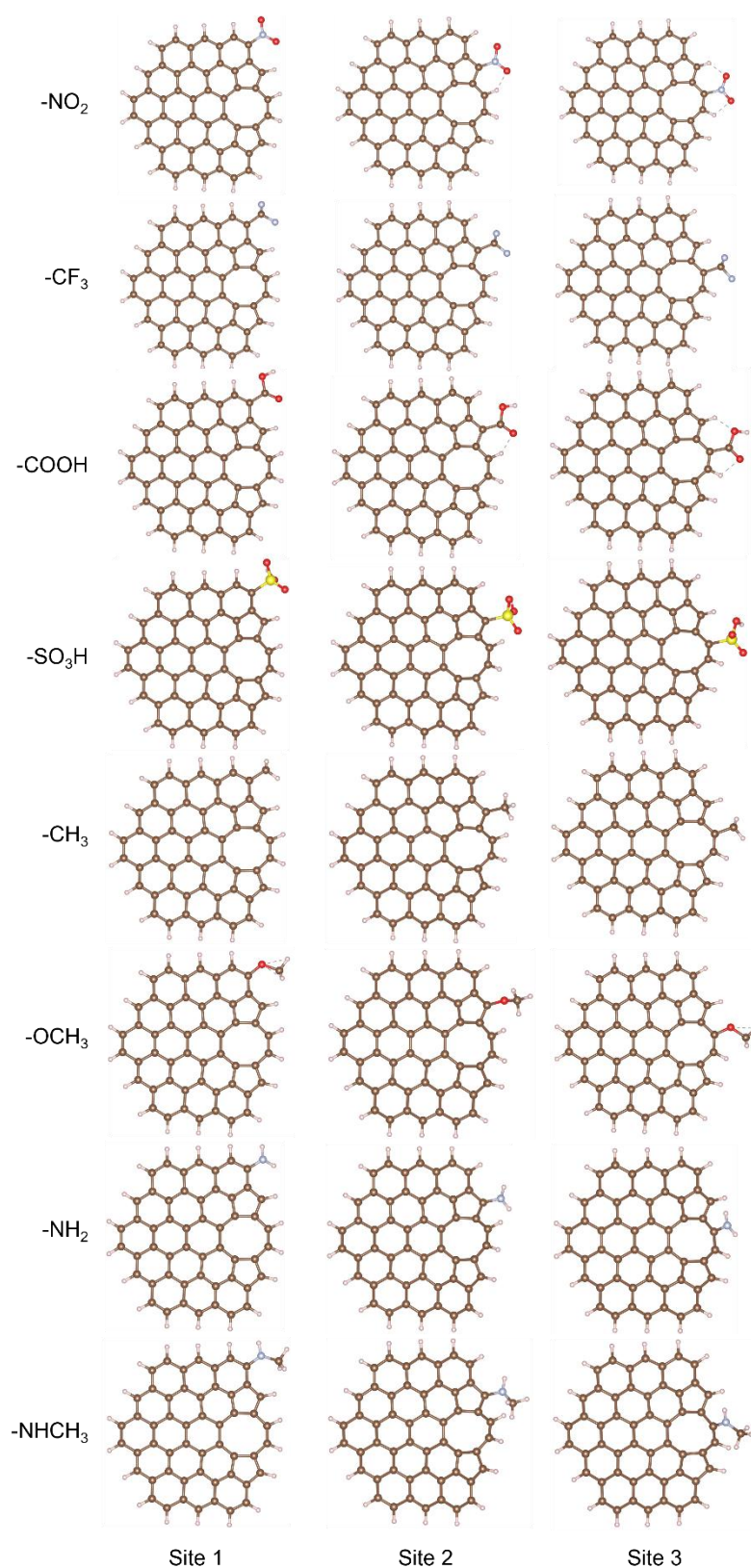
Figure S1. Top view of all the 24 kinds of designed FDCs in this work. Three adsorption sites (Site 1, Site 2, and Site 3) near or in the 585 defects were selected for the functionalization.
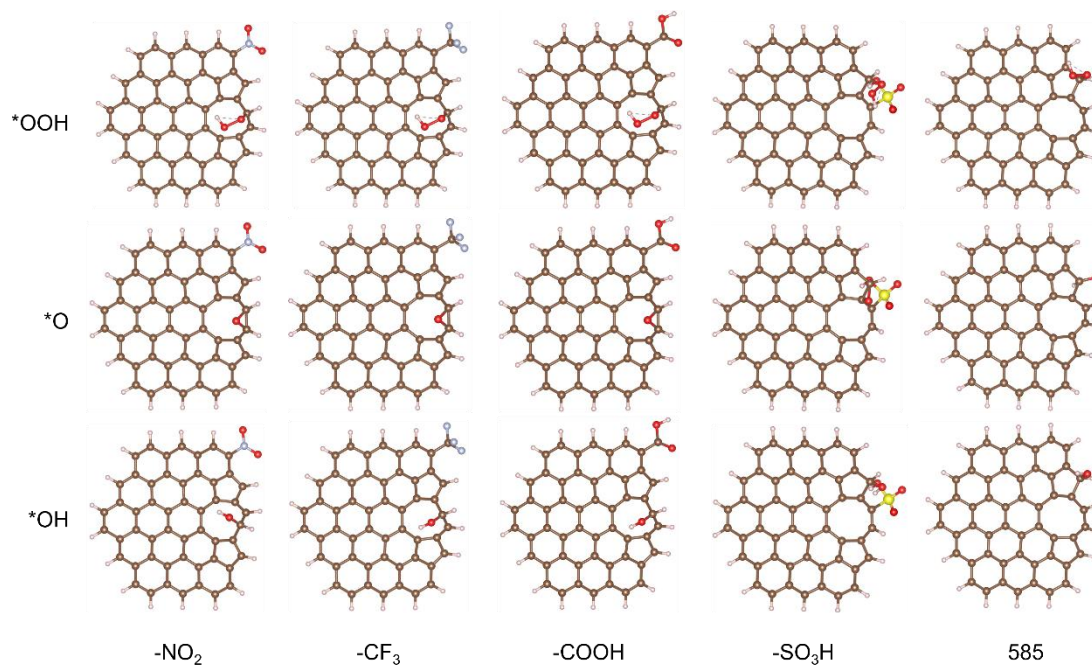
Figure S2. The top view of the electron-donating substituents functionalized 585 defects and pristine 585 defect with ORR intermediate adsorbed.
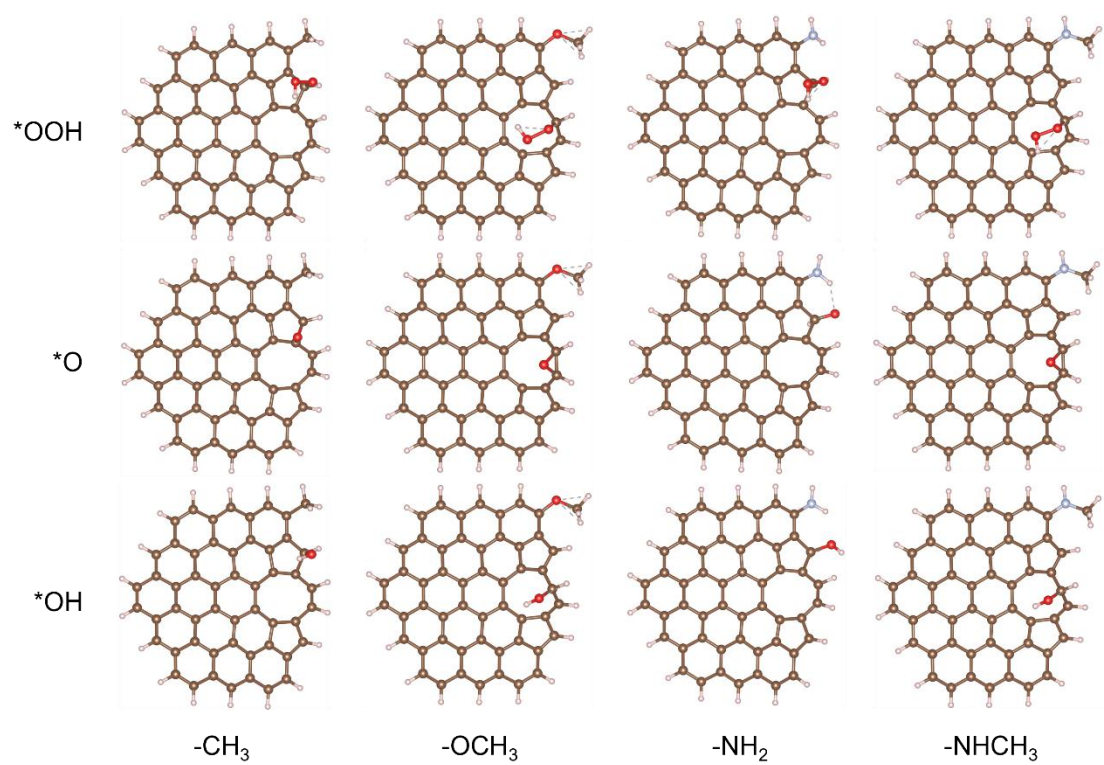
Figure S3. The top view of the electron-donating substituents functionalized 585 defects with ORR intermediate adsorbed.
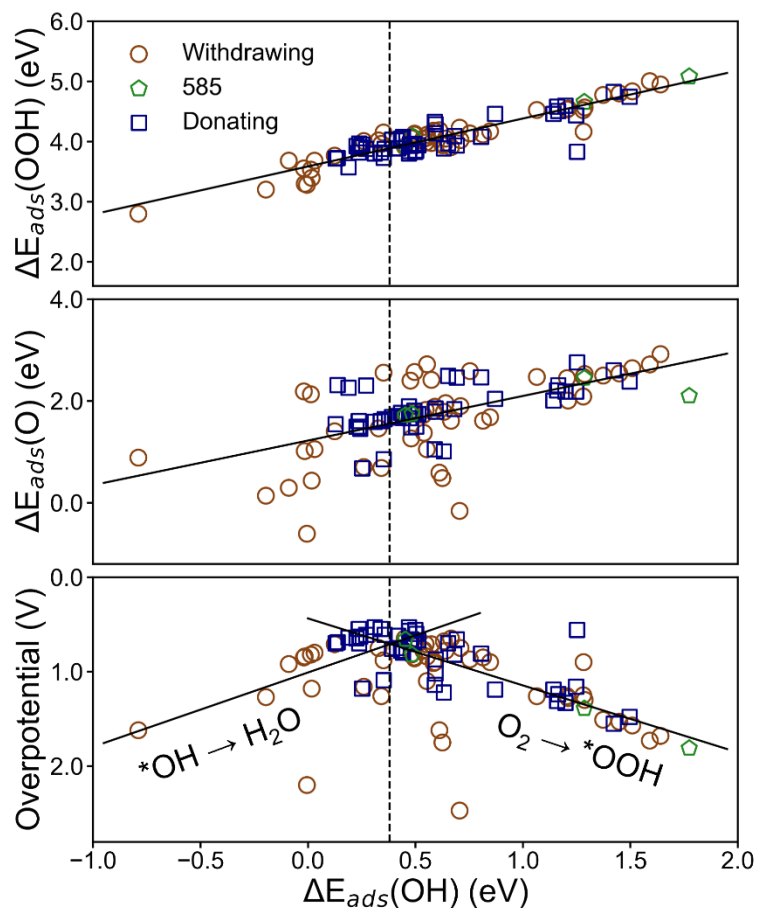
Figure S4. Liner scaling relationship between $\Delta E_{ads}(OOH)$ *vs.* $\Delta E_{ads}(OH)$ (top) and between $\Delta E_{ads}(O)$ *vs.* $\Delta E_{ads}(OH)$ (middle), i.e., $\Delta E_{ads}(OOH) = 0.8 * \Delta E_{ads}(OH) + 3.58$ and $\Delta E_{ads}(O) = 1.22 * \Delta E_{ads}(OH) + 0.88$. And volcano plot of ORR overpotential *vs.* $\Delta E_{ads}(OH)$ (bottom), the black dashed line divides the figure into two areas based on potential-determining steps.
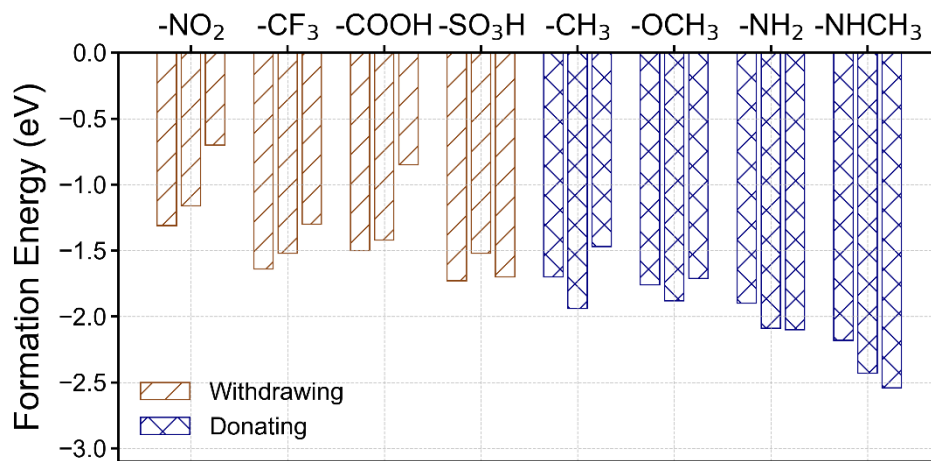
Figure S5. The formation energies of all the 24 kinds of designed FDCs.

-CF$_3$ -COOH   -SO$_3$H

-CH$_3$ -OCH$_3$ -NH$_2$
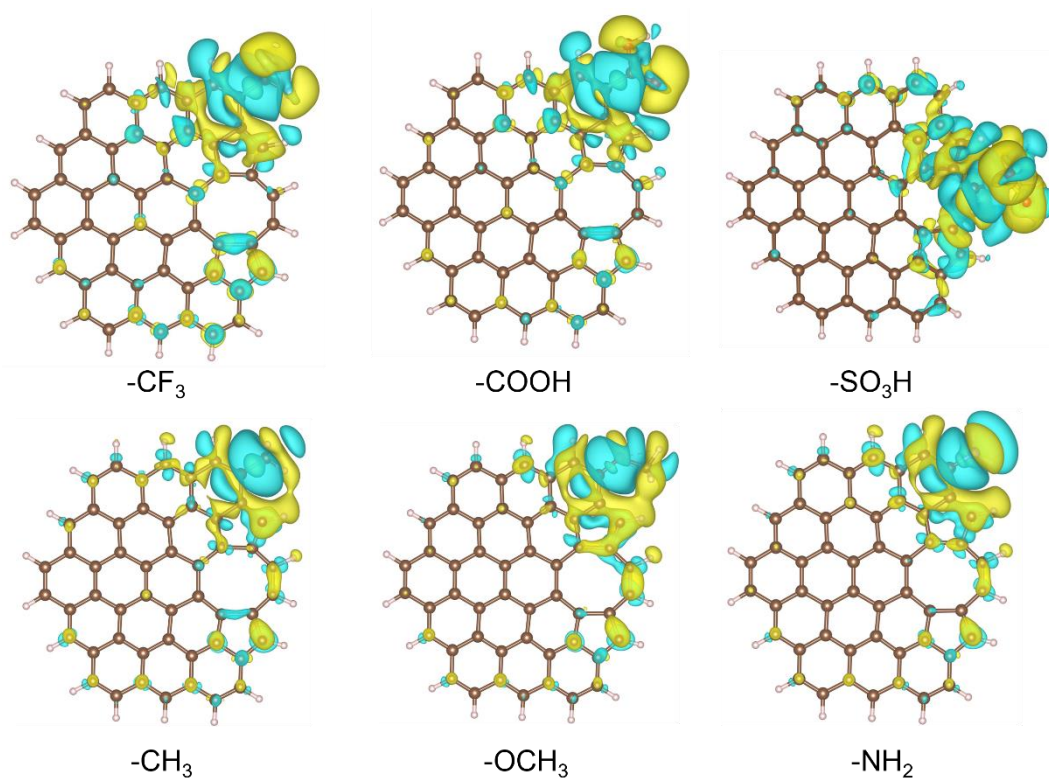
Figure S6. Differential charge density distributions of designed FDCs. The yellow and blue colours represent electron accumulation and depletion regions, respectively. The isosurface value is 3×10^{-4} e/Å^3.
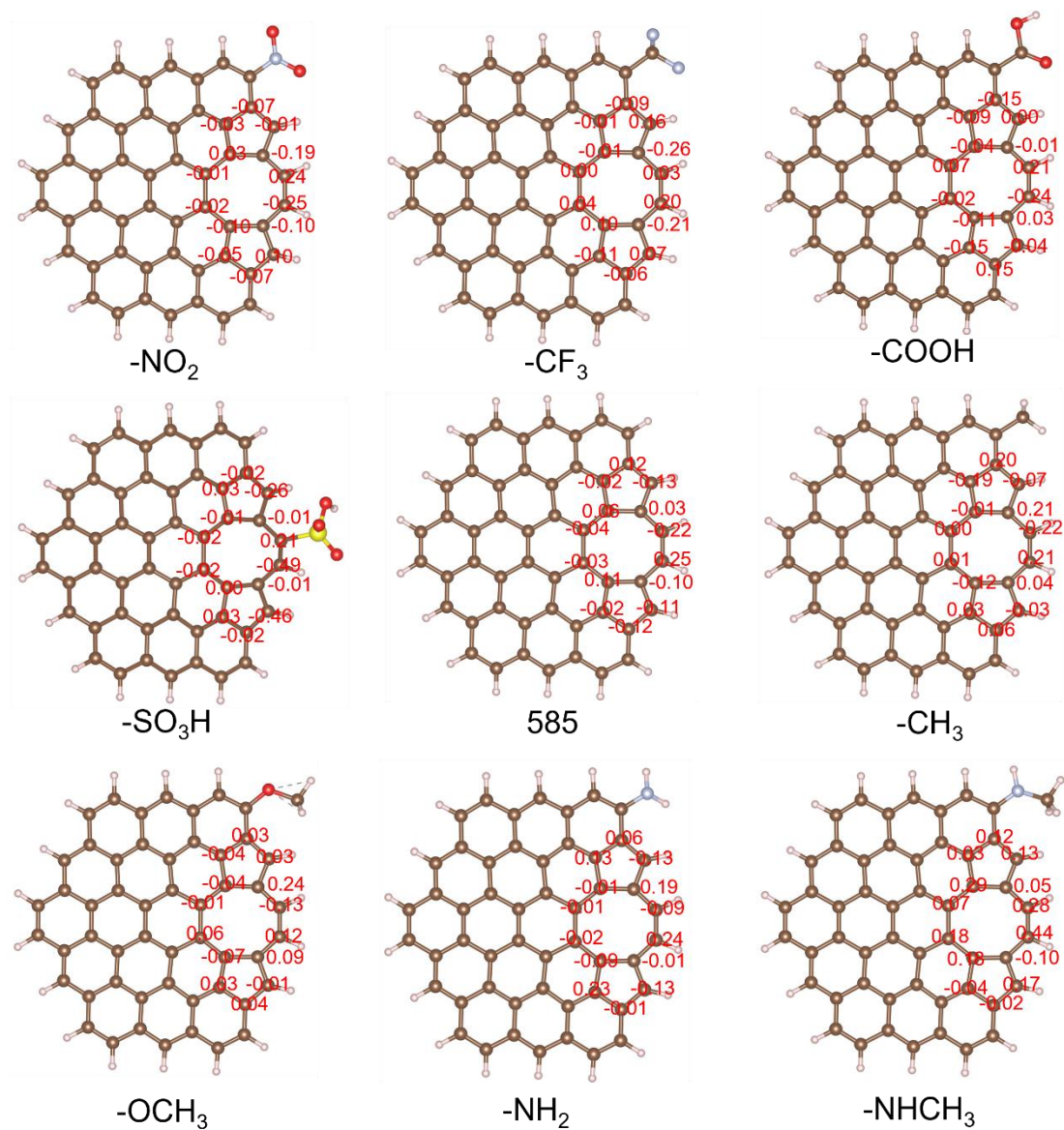
Figure S7. The Bader charge analysis results of carbon atoms among 585 defects.
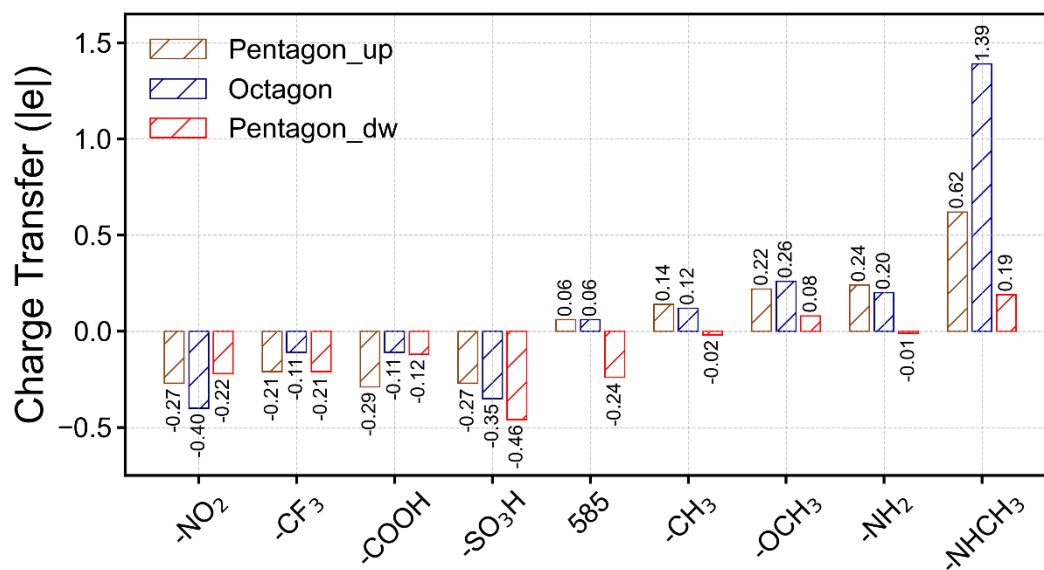
Figure S8. The electron gains (positive values) and loss (negative values) of carbon rings among 585 defects. Pentagon_up represents the upper pentagon ring of 585 defect, and Pentagon_dw represents the lower one.
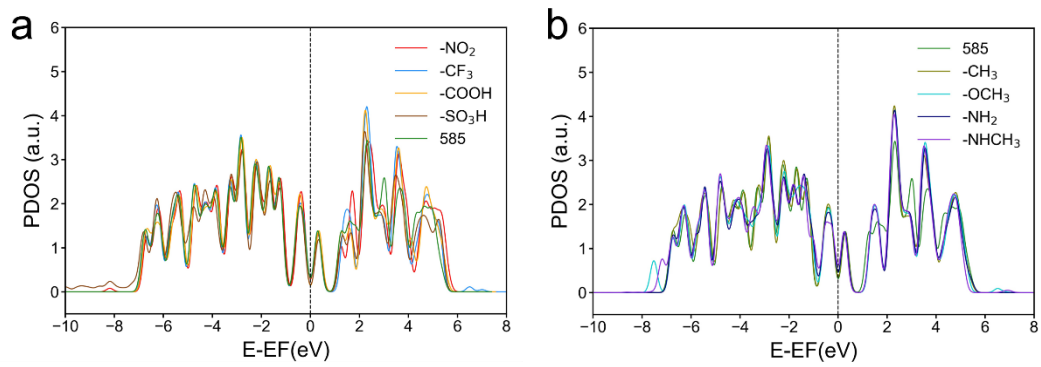
Figure S9. The PDOS of p_z orbital of carbon atoms in (a) electron-withdrawing groups and (b) electron-donating groups functionalized 585 defects. The black dashed lines represent Fermi level relative to vacuum.
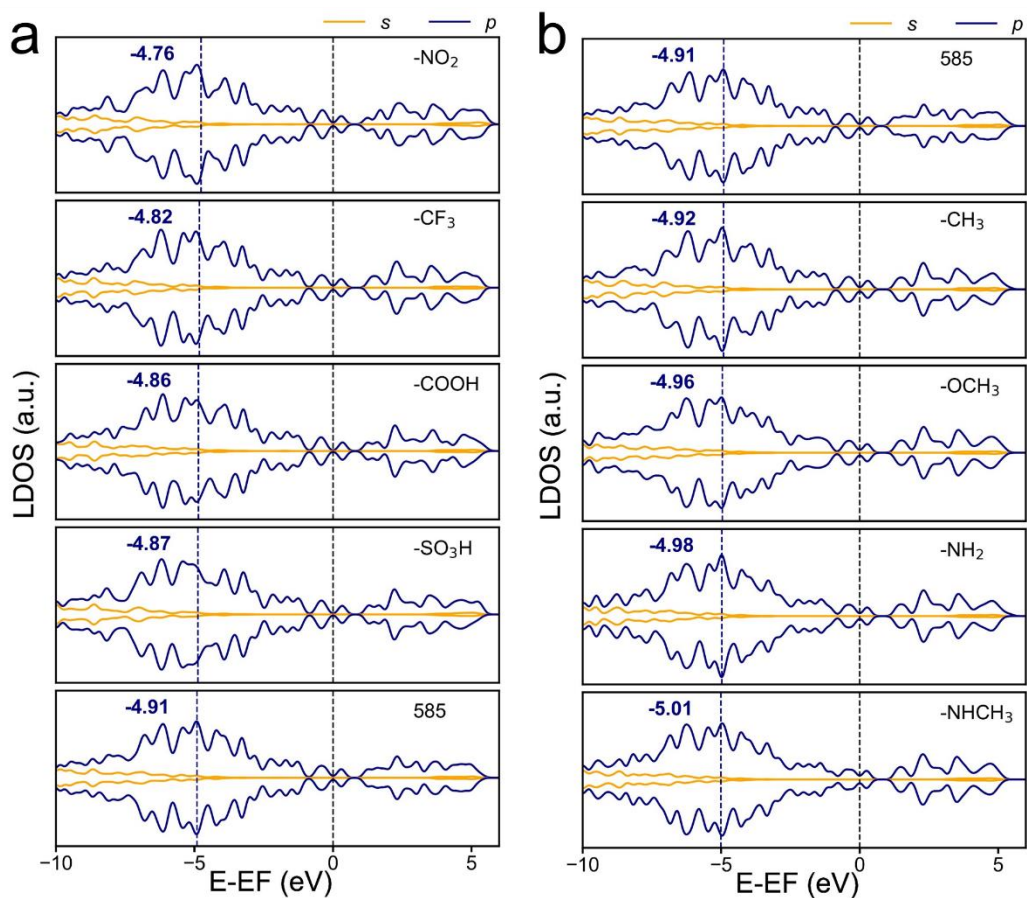
Figure S10. The LDOS of carbon atoms in (a) electron-withdrawing groups and (b) electron-donating groups functionalized 585 defects. The black dashed lines represent Fermi level relative to vacuum, the dashed lines and inserted numbers in navy color represent the *p* band center of each FDCs.
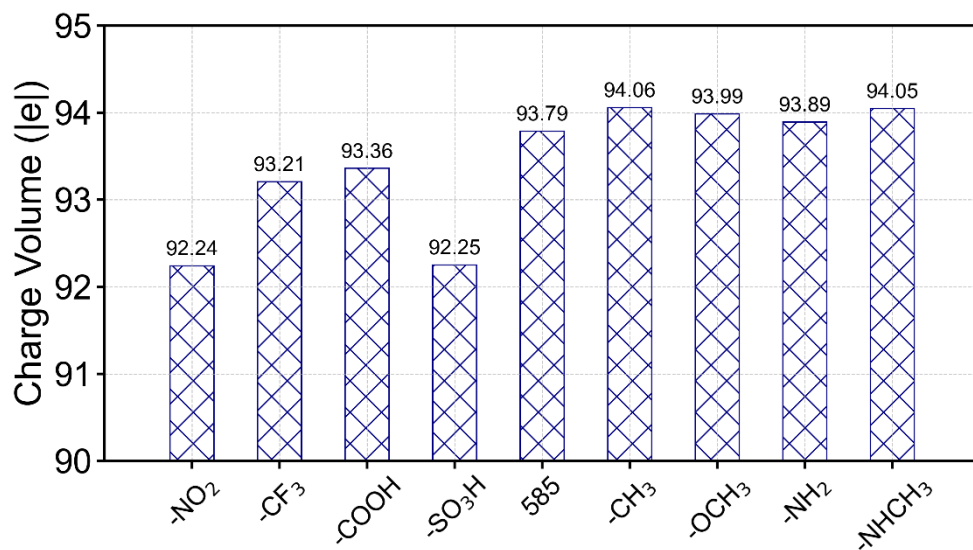
Figure S11. The electron volume of p orbitals of carbon atoms in FDCs.
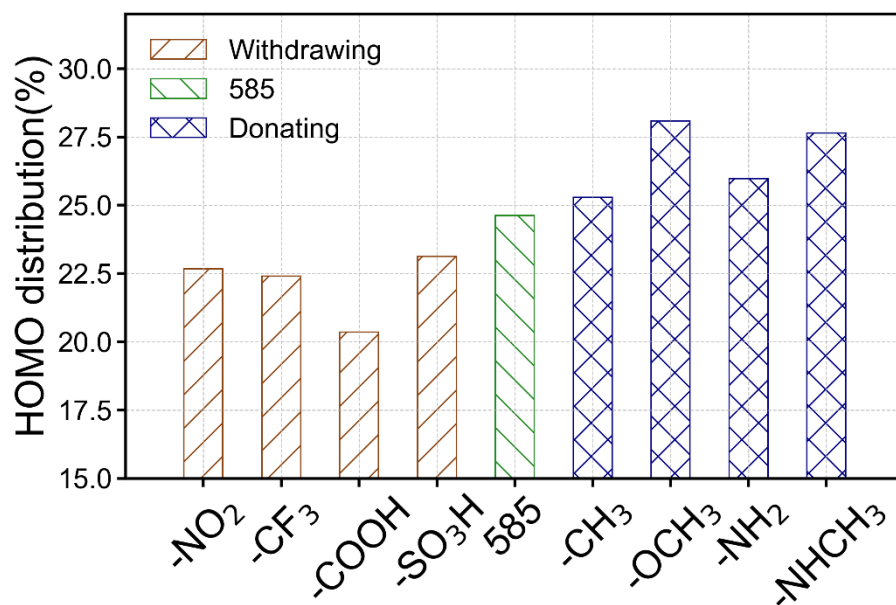
Figure S12. The contribution from carbon atoms near defects to the HOMO of designed FDCs.
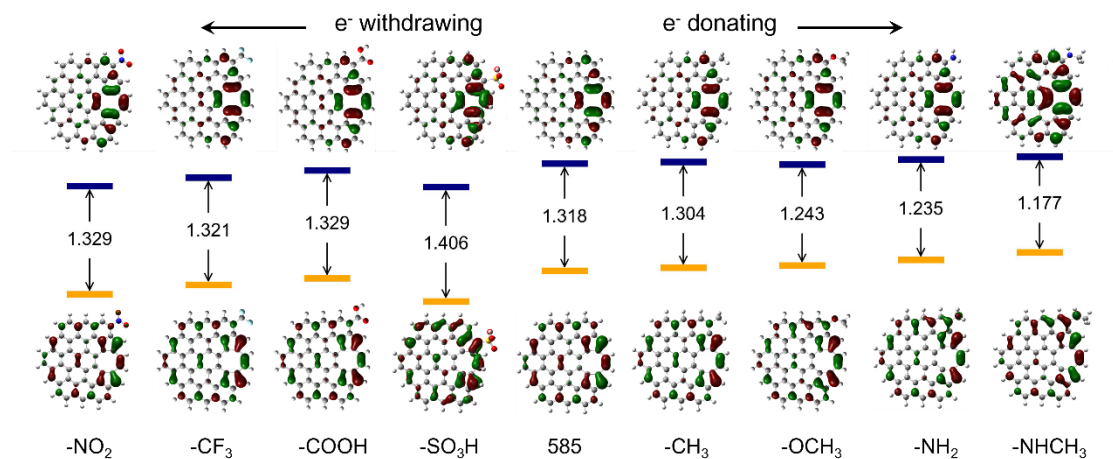
Figure S13. The HOMOs (bottom), LUMOs (upper), and band gaps of designed FDCs and pristine 585 defect.

The highest occupied molecular orbital (HOMO), lowest unoccupied molecular orbital (LUMO), and band gap of FDCs were calculated accurately at the level of B3LYP/6-31G*. As shown in Figure S13, electron-withdrawing substituents will expand the band gap and electron-donating substituents will narrow the band gap. For example, the band gap of 585-NO_2 and 585-$NHCH_3$ are 0.011 eV wider and 0.201 eV narrower than that of pristine 585 defects (1.318 eV), respectively. Furthermore, the coordination of electron-donating substituents will move both HOMOs and LUMOs to higher energy levels. Thus, electron-donating substituents not only can increase the ORR activity but also can boost the reaction kinetic. Moreover, all of the FDCs exhibit superior electron delocalization on HOMOs due to the existence of defects. Among them, electron-donating substituents can further induce the asymmetric orbital distribution around the carbon defects. As shown in Figure S9, the carbon atoms around electron-donating substituents generally show more contribution to HOMO than those near electron-withdrawing substituents. Combined with the electrostatic potential surface maps of the FDCs (Figure S14), the introduction of substituents can induce non-uniform charge distribution and make the carbon defects possess higher dipole moment, facilitating the electron transfer from HOMOs to the O_2 molecule and enhancing their electrocatalytic activities.[22-24]
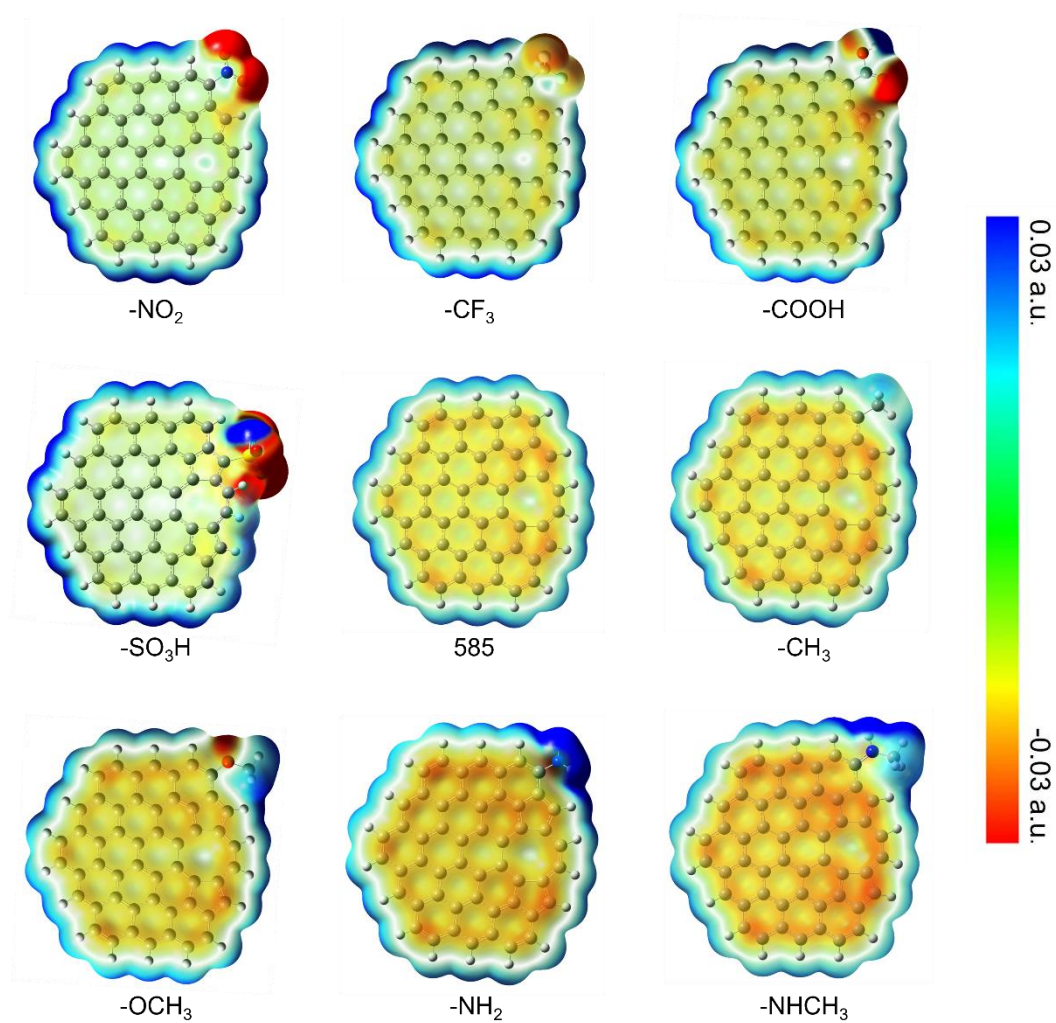
Figure S14. The electrostatic potential surface maps of designed FDCs and pristine 585 defect.
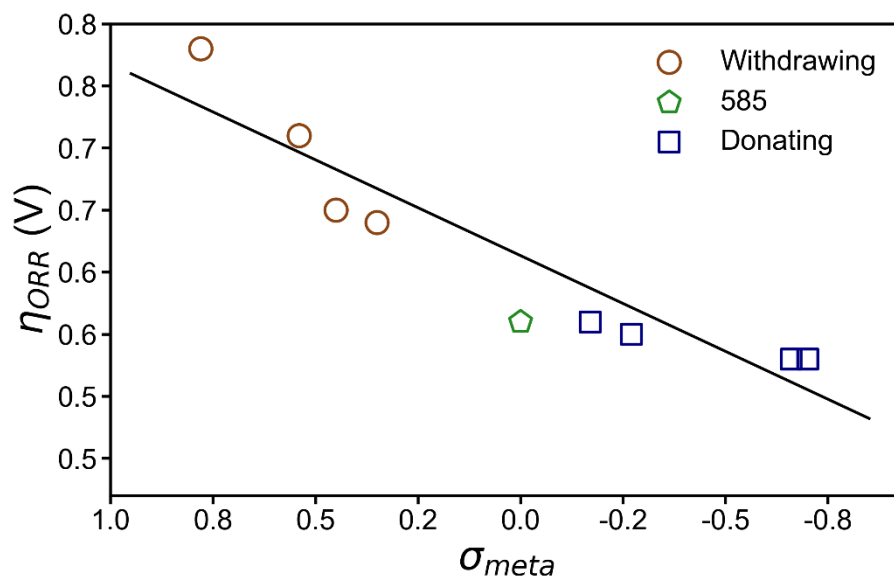
Figure S15. The linear relationship between substituent constants of substituents and ORR overpotential of FDCs.

Table S1. The Substituent constants (σ_{meta}) of the selected substituents.

Substituents	Electron-withdrawing				Electron-donating			
	NO_2	CF_3	COOH	SO_3H	CH_3	OCH_3	NH_2	$NHCH_3$
σ_{meta}	0.78	0.54	0.45	0.35	-0.17	-0.27	-0.66	-0.70

Table S2. The ORR intermediates adsorption energies (ΔE_{ads}, Eq. S7 - S9), the calculated ORR overpotential (η_{ORR}), and potential-determining step (PDS) on 585-NO_2. The data of best ORR activity of each substituent adsorbed site are in bold.

Catalyst	Ligand site	Active site	ΔE_{ads} (eV) *OOH	ΔE_{ads} (eV) *O	ΔE_{ads} (eV) *OH	η_{ORR} (V)	PDS
585-NO_2	1	**3**	**4.09**	**1.81**	**0.75**	**0.82**	*OOH
		4	4.18	1.80	0.58	0.91	*OOH
		5	4.05	1.73	0.54	0.78	*OOH
		6	4.52	2.09	1.28	1.25	*OOH
		7	4.32	1.80	0.58	1.05	*OOH
	2	2	4.53	2.47	1.06	1.26	*OOH
		4	**4.19**	**0.59**	**0.61**	**0.92**	*OOH
		5	4.23	-0.16	0.71	0.96	*OOH
		6	4.53	2.45	1.21	1.26	*OOH
	3	3	3.30	1.02	-0.01	0.84	*
		4	2.80	0.89	-0.79	1.62	*
		5	3.20	0.14	-0.20	1.26	*OH
		6	**3.53**	**2.13**	**0.01**	**0.83**	*
		7	3.40	0.43	0.02	1.19	*OH

Table S3. The ORR intermediates adsorption energies (ΔE_{ads}, Eq. S7 - S9), the calculated ORR overpotential (η_{ORR}), and potential-determining step (PDS) on 585-CF$_3$. The data of best ORR activity of each substituent adsorbed site are in bold.

Catalyst	Ligand site	Active site	ΔE_{ads} (eV) *OOH	*O	*OH	η_{ORR} (V)	PDS
585-CF₃	1	2	4.82	2.13	1.53	1.55	*OOH
		3	4.02	1.90	0.71	0.75	*OOH
		4	4.17	1.89	0.59	0.90	*OOH
		5	**3.98**	**1.82**	**0.55**	**0.71**	*OOH
		6	4.80	2.54	1.45	1.53	*OOH
	2	2	4.89	2.19	1.44	1.62	*OOH
		3	**3.99**	**2.14**	**0.49**	**0.72**	*OOH
		4	4.12	1.79	0.49	0.85	*OOH
		5	4.13	2.57	0.50	0.86	*OOH
		6	4.78	2.50	1.37	1.51	*OOH
	3	3	4.06	1.26	0.48	0.79	*OOH
		4	**4.02**	**1.46**	**0.33**	**0.75**	*OOH
		5	4.04	1.37	0.54	0.77	*OOH
		6	4.15	2.56	0.35	0.88	*OOH
		7	4.01	0.70	0.26	1.16	*OH

Table S4. The ORR intermediates adsorption energies (ΔE_{ads}, Eq. S7 - S9), the calculated ORR overpotential (η_{ORR}), and potential-determining step (PDS) on 585-COOH. The data of best ORR activity of each substituent adsorbed site are in bold.

Catalyst	Ligand site	Active site	ΔE_{ads} (eV)			η_{ORR} (V)	PDS
			*OOH	*O	*OH		
585-COOH	1	2	4.71	1.98	1.38	1.44	*OOH
		3	3.95	1.79	0.63	0.68	*OOH
		4	4.08	1.78	0.48	0.80	*OOH
		5	**3.92**	**1.73**	**0.45**	**0.65**	*OOH
		6	4.00	1.78	0.53	0.73	*OOH
		7	4.13	1.90	0.73	0.85	*OOH
	2	2	4.57	2.53	1.29	1.30	*OOH
		3	4.14	2.59	0.75	0.87	*OOH
		4	3.96	0.68	0.34	1.26	*OH
		5	**3.94**	**2.40**	**0.48**	**0.67**	*OOH
		6	4.17	2.47	1.28	0.90	*OOH
	3	3	3.28	-0.61	0.00	2.21	*OH
		4	3.68	1.05	0.03	0.80	*
		5	**3.77**	**1.40**	**0.12**	**0.71**	*
		6	3.55	2.19	-0.02	0.85	*OOH
		7	4.17	1.68	0.85	0.90	*OH

Table S5. The ORR intermediates adsorption energies (ΔE_{ads}, Eq. S7 - S9), the calculated ORR overpotential (η_{ORR}), and potential-determining step (PDS) on 585-SO$_3$H. The data of best ORR activity of each substituent adsorbed site are in bold.

Catalyst	Ligand site	Active site	ΔE_{ads} (eV)			η_{ORR} (V)	PDS
			*OOH	*O	*OH		
585-SO₃H	1	2	4.88	2.21	1.48	1.61	*OOH
		3	**4.05**	**1.96**	**0.64**	**0.78**	*OOH
		5	3.94	0.48	0.63	1.75	*OOH
		6	4.84	2.64	1.51	1.57	*OOH
	2	2	4.95	2.92	1.64	1.68	*OOH
		4	**4.06**	**1.05**	**0.55**	**1.10**	*OH
		6	5.00	2.72	1.59	1.73	*OOH
	3	**3**	**3.91**	**1.61**	**0.57**	**0.64**	*OH
		5	3.98	2.41	0.57	0.71	*OOH
		6	4.11	2.72	0.55	0.84	*OOH
		7	4.17	1.68	0.85	0.90	*OH

Table S6. The ORR intermediates adsorption energies (ΔE_{ads}, Eq. S7 - S9), the calculated ORR overpotential (η_{ORR}), and potential-determining step (PDS) on pristine 585. The data of best ORR activity of each substituent adsorbed site are in bold.

Catalyst	Ligand site	Active site	ΔE_{ads} (eV)			η_{ORR} (V)	PDS
			*OOH	*O	*OH		
585	N/A	**3**	**3.89**	**2.17**	**0.54**	**0.62**	*OOH
		4	4.09	1.75	0.48	0.82	*OOH
		5	3.93	1.72	0.45	0.66	*OOH
		6	5.08	2.10	1.77	1.81	*OOH
		7	4.66	2.45	1.29	1.39	*OOH

Table S7. The ORR intermediates adsorption energies (ΔE_{ads}, Eq. S7 - S9), the calculated ORR overpotential (η_{ORR}), and potential-determining step (PDS) on 585-CH$_3$. The data of best ORR activity of each substituent adsorbed site are in bold.

Catalyst	Ligand site	Active site	ΔE_{ads} (eV)			η_{ORR} (V)	PDS
			*OOH	*O	*OH		
585-CH$_3$	1	2	4.64	2.61	1.34	1.37	*OOH
		3	**3.83**	**1.74**	**0.50**	**0.56**	*OOH
		5	4.02	1.71	0.41	0.75	*OOH
		6	3.89	1.68	0.42	0.62	*OOH
	2	**3**	**3.97**	**2.49**	**0.65**	**0.70**	*OOH
		4	3.89	1.01	0.63	1.22	*OH
		6	4.82	2.60	1.42	1.55	*OOH
	3	3	3.85	1.50	0.50	0.60	*OH
		4	3.97	1.50	0.24	0.70	*OOH
		5	**3.82**	**1.60**	**0.24**	**0.59**	*
		6	3.73	2.31	0.14	0.69	*
		7	3.92	1.49	0.23	0.65	*OOH

Table S8. The ORR intermediates adsorption energies (ΔE_{ads}, Eq. S7 - S9), the calculated ORR overpotential (η_{ORR}), and potential-determining step (PDS) on 585-OCH_3. The data of best ORR activity of each substituent adsorbed site are in bold.

Catalyst	Ligand site	Active site	ΔE_{ads} (eV)			η_{ORR} (V)	PDS
			*OOH	*O	*OH		
585-OCH₃	1	2	4.68	2.55	1.34	1.41	*OOH
		3	3.84	1.66	0.47	0.57	*OOH
		4	4.07	1.66	0.44	0.80	*OOH
		5	**3.82**	**1.61**	**0.34**	**0.55**	*OOH
		6	3.91	1.67	0.41	0.64	*OOH
	2	**3**	**3.94**	**1.74**	**0.51**	**0.67**	*OOH
		4	3.73	0.86	0.35	1.09	*OH
		5	3.95	1.75	0.47	0.68	*OOH
		6	4.43	2.18	1.25	1.16	*OOH
	3	3	3.93	1.48	0.48	0.66	*OOH
		4	3.95	0.67	0.25	1.16	*OH
		5	3.57	2.26	0.19	0.64	*
		6	3.72	1.55	0.13	0.70	*
		7	**3.90**	**1.46**	**0.24**	**0.63**	*OOH

Table S9. The ORR intermediates adsorption energies (ΔE_{ads}, Eq. S7 - S9), the calculated ORR overpotential (η_{ORR}), and potential-determining step (PDS) on 585-NH$_2$. The data of best ORR activity of each substituent adsorbed site are in bold.

Catalyst	Ligand site	Active site	ΔE_{ads} (eV)			η_{ORR} (V)	PDS
			*OOH	*O	*OH		
585-NH$_2$	1	2	4.62	2.76	1.28	1.35	*OOH
		3	**3.80**	**1.89**	**0.47**	**0.53**	*OOH
		4	4.05	1.77	0.43	0.78	*OOH
		5	3.89	1.67	0.42	0.62	*OOH
		6	4.07	1.77	0.46	0.80	*OOH
	2	3	4.08	2.47	0.81	0.81	*OOH
		5	**3.96**	**1.81**	**0.49**	**0.69**	*OOH
		6	4.60	2.18	1.20	1.33	*OOH
	3	4	4.33	1.05	0.59	1.16	*OH
		6	**3.88**	**2.30**	**0.27**	**0.61**	*OOH
		7	4.29	1.85	0.59	1.02	*OOH

Table S10. The ORR intermediates adsorption energies (ΔE_{ads}, Eq. S7 - S9), the calculated ORR overpotential (η_{ORR}), and potential-determining step (PDS) on 585-NHCH$_3$. The data of best ORR activity of each substituent adsorbed site are in bold.

Catalyst	Ligand site	Active site	ΔE_{ads} (eV)			η_{ORR} (V)	PDS
			*OOH	*O	*OH		
585-NHCH$_3$	1	2	4.59	2.76	1.25	1.32	*OOH
		3	3.83	2.76	1.25	0.56	*OOH
		4	4.03	1.68	0.39	0.76	*OOH
		5	**3.80**	**1.59**	**0.31**	**0.53**	*OOH
		6	3.96	1.62	0.41	0.72	*OOH
	2	**3**	**3.93**	**2.46**	**0.69**	**0.66**	*OOH
		4	4.14	1.79	0.59	0.87	*OOH
		5	4.07	1.66	0.57	0.80	*OOH
		6	4.58	2.21	1.16	1.31	*OOH
	3	3	4.09	1.84	0.68	0.82	*OOH
		4	4.46	2.04	0.87	1.19	*OOH
		6	**3.88**	**1.64**	**0.36**	**0.61**	*OOH

Table S11. Change of the free energy coming from the differences in zero-point energies, ΔZPE, and entropy ΔS for the different reaction steps.[16]

Reaction Steps	Eq. S1	Eq. S2	Eq. S3	Eq. S4
Δ**ZPE - *T*Δ*S***	0.42	-0.39	0.37	-0.40

References:

1. Kresse, G.; Furthmüller, J., Efficiency of ab-initio total energy calculations for metals and semiconductors using a plane-wave basis set. *Comput. Mater. Sci.* **1996,** *6* (1), 15-50.

2. Kresse, G.; Furthmüller, J., Efficient iterative schemes for ab initio total-energy calculations using a plane-wave basis set. *Phys. Rev. B* **1996,** *54* (16), 11169-11186.

3. Blöchl, P. E., Projector augmented-wave method. *Phys. Rev. B* **1994,** *50* (24), 17953-17979.

4. Perdew, J. P.; Ernzerhof, M.; Burke, K., Rationale for mixing exact exchange with density functional approximations. *J. Chem. Phys.* **1996,** *105* (22), 9982-9985.

5. Perdew, J. P.; Burke, K.; Ernzerhof, M., Generalized Gradient Approximation Made Simple. *Phys. Rev. Lett.* **1996,** *77* (18), 3865-3868.

6. Grimme, S.; Antony, J.; Ehrlich, S.; Krieg, H., A consistent and accurate ab initio parametrization of density functional dispersion correction (DFT-D) for the 94 elements H-Pu. *J. Chem. Phys.* **2010,** *132* (15), 154104.

7. Grimme, S.; Ehrlich, S.; Goerigk, L., Effect of the damping function in dispersion corrected density functional theory. *J. Comput. Chem.* **2011,** *32* (7), 1456-1465.

8. Frisch, M. J.; Trucks, G. W.; Schlegel, H. B.; Scuseria, G. E.; Robb, M. A.; Cheeseman, J. R.; Scalmani, G.; Barone, V.; Petersson, G. A.; Nakatsuji, H.; Li, X.; Caricato, M.; Marenich, A. V.; Bloino, J.; Janesko, B. G.; Gomperts, R.; Mennucci, B.; Hratchian, H. P.; Ortiz, J. V.; Izmaylov, A. F.; Sonnenberg, J. L.; Williams; Ding, F.; Lipparini, F.; Egidi, F.; Goings, J.; Peng, B.; Petrone, A.; Henderson, T.; Ranasinghe, D.; Zakrzewski, V. G.; Gao, J.; Rega, N.; Zheng, G.; Liang, W.; Hada, M.; Ehara, M.; Toyota, K.; Fukuda, R.; Hasegawa, J.; Ishida, M.; Nakajima, T.; Honda, Y.; Kitao, O.; Nakai, H.; Vreven, T.; Throssell, K.; Montgomery Jr., J. A.; Peralta, J. E.; Ogliaro, F.; Bearpark, M. J.; Heyd, J. J.; Brothers, E. N.; Kudin, K. N.; Staroverov, V. N.; Keith, T. A.; Kobayashi, R.; Normand, J.; Raghavachari, K.; Rendell, A. P.; Burant, J. C.; Iyengar, S. S.; Tomasi, J.; Cossi, M.; Millam, J. M.; Klene, M.; Adamo, C.; Cammi, R.; Ochterski, J. W.; Martin, R. L.; Morokuma, K.; Farkas, O.; Foresman, J. B.; Fox, D. J. *Gaussian 16 Rev. C.01*, Wallingford, CT, 2016.

9. Wang, V.; Xu, N.; Liu, J.-C.; Tang, G.; Geng, W.-T., VASPKIT: A user-friendly interface facilitating high-throughput computing and analysis using VASP code. *Comput. Phys. Commun.* **2021,** *267*, 108033.

10. Sanville, E.; Kenny, S. D.; Smith, R.; Henkelman, G., Improved grid-based algorithm for Bader charge allocation. *J. Comput. Chem.* **2007,** *28* (5), 899-908.

11. Lu, T.; Chen, F., Multiwfn: A multifunctional wavefunction analyzer. *J. Comput. Chem.* **2012,** *33* (5), 580-592.

12. Momma, K.; Izumi, F., VESTA: a three-dimensional visualization system for electronic and structural analysis. *J. Appl. Crystallogr.* **2008,** *41* (3), 653-658.

13. Hjorth Larsen, A.; Jorgen Mortensen, J.; Blomqvist, J.; Castelli, I. E.; Christensen, R.; Dulak, M.; Friis, J.; Groves, M. N.; Hammer, B.; Hargus, C.; Hermes, E. D.; Jennings, P. C.; Bjerre Jensen, P.; Kermode, J.; Kitchin, J. R.; Leonhard Kolsbjerg, E.; Kubal, J.; Kaasbjerg, K.; Lysgaard, S.; Bergmann

Maronsson, J.; Maxson, T.; Olsen, T.; Pastewka, L.; Peterson, A.; Rostgaard, C.; Schiotz, J.; Schutt, O.; Strange, M.; Thygesen, K. S.; Vegge, T.; Vilhelmsen, L.; Walter, M.; Zeng, Z.; Jacobsen, K. W., The atomic simulation environment-a Python library for working with atoms. *J Phys Condens Matter* **2017,** *29* (27), 273002.

14. J. K. Nørskov; J. Rossmeisl; A. Logadottir; Lindqvist, a. L., Origin of the Overpotential for Oxygen Reduction at a Fuel-Cell Cathode. *J. Phys. Chem. B* **2004,** *108*.

15. Rossmeisl, J.; Logadottir, A.; Nørskov, J. K., Electrolysis of water on (oxidized) metal surfaces. *Chem. Phys.* **2005,** *319* (1), 178-184.

16. Valdés, Á.; Qu, Z. W.; Kroes, G. J.; Rossmeisl, J.; Nørskov, J. K., Oxidation and Photo-Oxidation of Water on TiO2 Surface. *J. Phys. Chem. C* **2008,** *112* (26), 9872-9879.

17. Mathew, K.; Kolluru, V. S. C.; Mula, S.; Steinmann, S. N.; Hennig, R. G., Implicit self-consistent electrolyte model in plane-wave density-functional theory. *J. Chem. Phys.* **2019,** *151* (23), 234101.

18. Mathew, K.; Sundararaman, R.; Letchworth-Weaver, K.; Arias, T. A.; Hennig, R. G., Implicit solvation model for density-functional study of nanocrystal surfaces and reaction pathways. *J. Chem. Phys.* **2014,** *140* (8), 084106.

19. Zhou, S.; Yang, X.; Pei, W.; Liu, N.; Zhao, J., Heterostructures of MXenes and N-doped graphene as highly active bifunctional electrocatalysts. *Nanoscale* **2018,** *10* (23), 10876-10883.

20. Pei, W.; Zhou, S.; Bai, Y.; Zhao, J., N-doped graphitic carbon materials hybridized with transition metals (compounds) for hydrogen evolution reaction: Understanding the synergistic effect from atomistic level. *Carbon* **2018,** *133*, 260-266.

21. Hoffmann, R., An Extended Hückel Theory. I. Hydrocarbons. *J. Chem. Phys.* **2004,** *39* (6), 1397-1412.

22. Li, D.; Wang, B.; Long, X.; Xu, W.; Xia, Y.; Yang, D.; Yao, X., Controlled Asymmetric Charge Distribution of Active Centers in Conjugated Polymers for Oxygen Reduction. *Angew. Chem. Int. Ed.* **2021,** *60* (51), 26483-26488.

23. Long, X.; Li, D.; Wang, B.; Jiang, Z.; Xu, W.; Wang, B.; Yang, D.; Xia, Y., Heterocyclization Strategy for Construction of Linear Conjugated Polymers: Efficient Metal-Free Electrocatalysts for Oxygen Reduction. *Angew. Chem. Int. Ed.* **2019,** *58* (33), 11369-11373.

24. Chen, X.; Qiao, Q.; An, L.; Xia, D., Why Do Boron and Nitrogen Doped α- and γ-Graphyne Exhibit Different Oxygen Reduction Mechanism? A First-Principles Study. *J. Phys. Chem. C* **2015,** *119* (21), 11493-11498.